

Drag force on an oscillatory spherical bubble in shear-thinning fluid

Xianping Zhang^{1,2,†}, Kazuyasu Sugiyama^{1,2} and Tomoaki Watamura^{2,3}

¹Graduate School of Engineering Science, Osaka University, 1-3, Machikaneyama, Toyonaka, Osaka 560-8531, Japan

²RIKEN, 2-1 Hirosawa, Wako, Saitama 351-0198, Japan

³Department of Mechanical Engineering, Kyoto Institute of Technology, Goshokaido-cho, Matsugasaki, Sakyo-ku, Kyoto 606-8585, Japan

(Received 15 July 2022; revised 15 December 2022; accepted 23 January 2023)

Power-law shear-thinning fluid motions induced by a translating spherical bubble with sinusoidal oscillation at a high frequency are numerically studied. We focus on reducing the time-averaged drag force D on the bubble owing to the oscillation-enhanced shear-thinning effect. Under the assumption of negligible convection, the unsteady Stokes equation is directly solved in a finite-difference manner over a wide parameter space of the dimensionless oscillation amplitude A (corresponding to the oscillatory-to-translational velocity ratio) and the power-law index n of the viscosity. The results show that, for small amplitude ($A \ll 1$), the drag reduction ratio $1 - D/D_0$ (here, D_0 is D with no oscillation) is proportional to A^2 . In contrast, for large amplitude ($A \gg 1$), the drag ratio D/D_0 is proportional to A^{n-1} , revealing a power-law behaviour. In the case of $A \gg 1$ for a strong shear-thinning fluid with small n , the square of the vorticity over the entire domain is much smaller than that of the shear rate, and thus the bulk flow may be regarded as irrotational. To provide a fundamental perspective on the drag reduction mechanism, a theoretical model is proposed based on potential theory, and demonstrated to well capture the power-law relation between D/D_0 and A .

Key words: bubble dynamics, rheology, drag reduction

1. Introduction

Shear-thinning fluids exist in a wide range of industrial processes such as air lubrication (Bobade *et al.* 2017; Selway, Chan & Stokes 2017), aeration (Samaras *et al.* 2014), airlift pumps, food processing (McClements 2004) and blood pumps (Moyers-Gonzalez, Owens & Fang 2009). Dispersions, such as drops (Ohta *et al.* 2003), bubbles (Premlata *et al.*

† Email address for correspondence: xianping.zhang@flow.me.es.osaka-u.ac.jp

2017) and particles are often found in shear-thinning fluid systems. To control the motion of the dispersion in the sedimentation process (Wang, Wang & Guo 2006) and the bubble (Iwata *et al.* 2008; Gaudron, Warnez & Johnsen 2015; De Corato *et al.* 2019*b*) or particle (Agi *et al.* 2020) removal process, mechanical vibration and ultrasonic irradiation are often applied. In addition to the utilization of the primary Bjerkness force (Eller 1968) that moves the bubble to the node or anti-node for the standing wave, such an oscillatory implementation alters the rheologic property owing to the non-Newtonian nature. As a result, the viscosity is spatially varied, the drag force on the dispersion is reduced and the composite feature of the bubbly or particulate system is modified.

Compared with Newtonian fluids, more complex physical changes may occur during the vibration or oscillation of the shear-thinning fluids. In internal flows, the vibration increases the volumetric flow rate depending on the amplitude and frequency (Barnes, Townsend & Walters 1969, 1971; Deysarkar & Turner 1981; Phan-Thien & Dudek 1982*a*; Siginer 1991; Deshpande & Barigou 2001). Deysarkar & Turner (1981) also have found flow rate enhancement of a normally stiff paste of fine iron ore and 16 % water flowing in a mechanically vibrated tube. When the pulsation of the driving pressure gradient is somewhat weak, the change in the flow rate is proportional to the square of the amplitude (Phan-Thien & Dudek 1982*a*). When the role of viscoelasticity is substantial, the flow enhancement becomes drastic at the resonant frequency (Andrienko, Siginer & Yanovsky 2000; Casanellas & Ortín 2011; Casanellas & Ortín 2012).

The dynamics of dispersions in resting shear-thinning fluids has been extensively investigated (Acharya, Mashelkar & Ulbrecht 1977; Dekee, Carreau & Mordarski 1986), well reviewed by Chhabra (2006) and Kulkarni & Joshi (2005) and has substantial differences from that in Newtonian fluid. The long-range disturbance caused by the moving sphere (Gu & Tanner 1985) is reduced due to the shear-thinning effect of the fluid. In flow around a spherical bubble with constant volume rising in a power-law shear-thinning fluid, in which the fluid velocity divided by the bubble radius corresponds to the characteristic shear rate scale and gives the characteristic viscosity, the drag on the bubble is reduced below the corresponding Newtonian value (Dhole, Chhabra & Eswaran 2007*a*). The local viscosity change greatly depends on the drop shape and is bound to impact the drop rise velocity (Ohta *et al.* 2003, 2005). The mass transfer around a bubble (Hirose & Moo-Young 1969; Michaelides 2006; Dhole, Chhabra & Eswaran 2007*b*; Radl, Tryggvason & Khinast 2007) or drop (Wellek & Gürkan 1976; Kishore, Chhabra & Eswaran 2007) is increased when the shear-thinning effect is enhanced. Besides, the wall effect induced by a confining tube on the flows around a rigid sphere is seen to be suppressed compared with that in a Newtonian fluid at fixed values of the Reynolds number and diameter ratio (Song, Gupta & Chhabra 2011).

The pulsation, oscillation and acoustic excitation increase the speed of a bubble (Stein & Buggisch 2000; Iwata *et al.* 2008; Karapetsas *et al.* 2019), drop (Mendoza-Fuentes *et al.* 2018) or particle (Iwamuro, Watamura & Sugiyama 2019), and significantly augment the rate of heat transfer in shear-thinning fluids (Gupta, Patel & Chhabra 2020, 2021; Mishra, Patel & Chhabra 2020; Mishra & Chhabra 2021). Qualitatively, the cause is attributed to the reduction in the effective viscosity. Pulsating the power-law shear-thinning fluid with relatively small oscillation amplitude ($0 \leq A \leq 0.8$) over a sphere (Mishra *et al.* 2020; Mishra & Chhabra 2021) or a cylinder (Gupta *et al.* 2020, 2021) promotes heat transfer compared with that in non-pulsating flows, which reveals the potential application of the pulsation or oscillation in controlling the heat transfer by varying the kinematic parameters of the flow. For a radially oscillating bubble in the Carreau–Yasuda fluid, De Corato, Dimakopoulos & Tsamopoulos (2019*a*) performed numerical simulations

under the assumption that the viscosity distribution obeys the spherically symmetric velocity gradient given by potential theory. They showed that the friction coefficient is proportional to C_u^{n-1} (here, C_u is the Carreau number and n is the shear-thinning index). In a viscoelastic agarose gel, the ultrasound irradiation changes the effective viscosity in the presence of bubbles, especially at the resonant frequency (Jamburidze *et al.* 2017). Although the drag reduction mechanism has been discussed in phenomenologically postulated ways, the detail is not fully clarified owing to the lack of comprehensive analyses.

Our objective is to provide a fundamental perspective on the drag reduction mechanism for oscillatory dispersion in a shear-thinning fluid at a high frequency. For a rigid particle, the oscillatory boundary layer forms near the no-slip wall (Majdalani & Van Moorhem 1997). At a sufficiently high frequency, a remarkably large vorticity is likely to be generated within a very thin boundary layer, making the multiscale system complex. We treat a spherical bubble with a free-slip boundary in the present study. In contrast to the volume change bubble (Iwata *et al.* 2008; De Corato *et al.* 2019a), the bubble volume remains constant. Neglecting the convective and compressible effects, we consider a creeping incompressible fluid and obtain the solution to the unsteady Stokes equation. Although the assumption of no volume change in the bubble is hypothetical, we choose the simplified system to extract the essence of the drag reduction mechanism. Note that, even for the steady creeping flow, the formulation of the drag force in a shear-thinning fluid (Slattery & Bird 1961; Hirose & Moo-Young 1969; Renaud, Mauret & Chhabra 2004) must rely on an approximation method because the nonlinearity in the non-Newtonian viscosity expression prevents us from deriving the analytical solution, unlike the case of a Newtonian flow. We perform numerical simulation and modelling for the flow of a well-defined power-law fluid induced by the bubble motion at the prescribed speed. Our research will shed light on the dynamics of bubbles in shear-thinning fluid subjected to ultrasonic irradiation or mechanical vibration.

The rest of this paper is organized as follows. We formulate the problem in § 2.1, comment on some essential parameters in § 2.2 and present some tests to validate the numerical method in § 2.3. In § 3, results are presented and discussed. We investigate the time-averaged velocity and viscosity distribution of the fluid around the bubble to overview the overall features of the fluid flow induced by the oscillatory bubble in § 3.1. In § 3.2, the dependence of the drag force on the power-law index and oscillation amplitude is examined. In § 3.3, we discuss the drag reduction mechanism and provide a theoretical model to predict the time-averaged drag force. In § 4, we provide some vital comments to conclude the paper.

2. Numerical simulation

2.1. General formulation

As shown in figure 1, we consider a spherical bubble with a radius a^* travelling along the x^* axis direction with a velocity of U^* . Hereafter, a superscript $*$ stands for a dimensional quantity. In the present study, the velocity U^* of the bubble consists of two parts: the constant part U_0^* , and the oscillatory part $U_0^*A \cos \omega^*t^*$ (here, A is the dimensionless oscillation amplitude, ω^* is the angular frequency and t^* is the time) which varies sinusoidally with time. The liquid is regarded as a power-law fluid, for which the viscosity μ^* is given by

$$\mu^* = K^* \dot{\gamma}^{*n-1}, \quad (2.1)$$

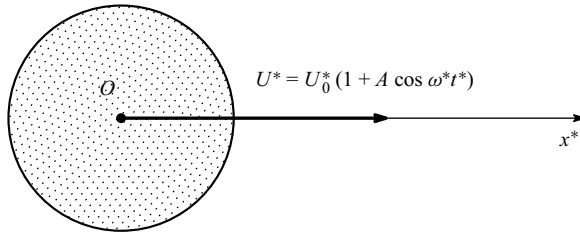


Figure 1. The schematic of the spherical oscillatory bubble travelling in shear-thinning fluid.

where K^* is the consistency factor, $\dot{\gamma}^*$ is the shear rate and n is the power-law index, which is limited to $0 < n < 1$ for the shear-thinning fluid. Note that although the power-law expression (2.1) with the constants K^* and n is usually obtained under steady conditions, it is applied to unsteady flows to facilitate elucidation of the drag reduction mechanism rather than to reproduce the actual phenomena. Upon choosing a^* , U_0^* , K^* and the density of fluid ρ^* , all the quantities are non-dimensionalized in a way such that

$$\left. \begin{aligned} U &= \frac{U^*}{U_0^*}, & \omega &= \frac{\omega^* \rho^* (a^*)^{n+1}}{K^* (U_0^*)^{n-1}}, & t &= \frac{t^* K^* (U_0^*)^{n-1}}{\rho^* (a^*)^{n+1}}, & \dot{\gamma} &= \frac{\dot{\gamma}^* a^*}{U_0^*}, \\ \mathbf{u} &= \frac{\mathbf{u}^*}{U_0^*}, & p &= \frac{p^* (a^*)^n}{K^* (U_0^*)^n}, & \boldsymbol{\tau} &= \frac{\boldsymbol{\tau}^* (a^*)^n}{K^* (U_0^*)^n}, & \mathbf{S} &= \frac{\mathbf{S}^* a^*}{U_0^*}, & \nabla &= a^* \nabla^*, \end{aligned} \right\} \quad (2.2)$$

where \mathbf{u} , p , $\boldsymbol{\tau}$, \mathbf{S} and ∇ respectively denote the fluid velocity vector, the pressure, the viscous stress tensor, the strain rate tensor and the nabla operator. The non-dimensional velocity of the bubble is

$$U = 1 + A \cos \omega t. \quad (2.3)$$

For the incompressible creeping fluid, the equation of continuity and the unsteady Stokes equation are expressed as

$$\nabla \cdot \mathbf{u} = 0, \quad (2.4)$$

$$\frac{\partial \mathbf{u}}{\partial t} = -\nabla p + \nabla \cdot \boldsymbol{\tau}. \quad (2.5)$$

The constitutive equations of the viscosity and the viscous stress tensor are

$$\mu = \dot{\gamma}^{n-1}, \quad \boldsymbol{\tau} = 2\mu \mathbf{S}, \quad (2.6a,b)$$

where

$$\mathbf{S} = \frac{1}{2}(\nabla \mathbf{u} + (\nabla \mathbf{u})^T), \quad \dot{\gamma} = \sqrt{2\mathbf{S} : \mathbf{S}}. \quad (2.7a,b)$$

On the bubble wall, we impose the kinematic and free-slip (FS) boundary conditions

$$\mathbf{n} \cdot \mathbf{u} = \mathbf{n} \cdot \mathbf{e}_x U, \quad (\boldsymbol{\tau} \cdot \mathbf{n}) \times \mathbf{n} = \mathbf{0} \text{ at } r = 1, \quad (2.8a,b)$$

where \mathbf{n} is the unit normal vector pointing outwards on the bubble, and \mathbf{e}_x is the unit vector in the x direction. At a sufficiently large distance from the bubble, the velocity and the pressure are $\mathbf{u} \rightarrow 0$ and $\partial p / \partial r \rightarrow 0$. The force F acting on the oscillatory bubble can be obtained by

$$F = -\mathbf{e}_x \cdot \oint_{r=1} (-p\mathbf{I} + \boldsymbol{\tau}) \cdot \mathbf{n} \, dS. \quad (2.9)$$

Drag force on an oscillatory spherical bubble

Note that three dimensionless parameters n , A and ω characterize the behaviour of the system in the present study. Thus, the conversion between the dimensionless and dimensional force (i.e. F and F^*) is referred to as

$$F = \frac{F^*(a^*)^{n-2}}{K^*(U_0^*)^n}. \quad (2.10)$$

2.2. Simulation method

We describe (2.4) and (2.5) in spherical coordinates. The second-order central difference method numerically discretizes the equation set on staggered grids over a two-dimensional domain. For time marching, we apply the second-order Crank–Nicolson method to the viscous term. A simplified-marker-and-cell algorithm (Amsden & Harlow 1970) satisfies the momentum equation (2.5) simultaneously with the solenoidal condition (2.4) by means of a direct solution to the pressure equation (Müller & Chan 2019).

We choose the dimensionless angular frequency ω and oscillation amplitude A by referring to experimental work using a spherical particle (Iwamuro *et al.* 2019). Considering the liquid density $\rho^* \sim 10^3 \text{ kg/m}^3$, the sound pressure amplitude $(\Delta p^*) \sim 10^5 \text{ Pa}$, the frequency $f^* \sim 10^5 \text{ s}^{-1}$ and the speed of sound $c^* \sim 10^3 \text{ m s}^{-1}$, the fluctuating acceleration amplitude is estimated as $(\Delta \alpha^*) \sim (\Delta p^*)f^*/(\rho^*c^*) \sim 10^4 \text{ m s}^{-2}$. The time-averaged acceleration corresponds to the gravitational acceleration $\mathcal{G} \sim 10^1 \text{ m s}^{-2}$. The ratio of the fluctuating force amplitude to the time-averaged drag force would be $(\Delta \alpha^*)/\mathcal{G} \sim 10^3$, which scales the dimensionless angular frequency ω . The typical fluctuating velocity amplitude in Iwamuro *et al.* (2019) is estimated as $U_0^*A \sim (\Delta p^*)/(\rho^*c^*) \sim 10^{-1} \text{ m s}^{-1}$, that is comparable to the fall speed U_0^* . Hence, the dimensionless oscillation amplitude A would be of order unity. In the present study, the dimensionless angular frequency is fixed at $\omega = 1 \times 10^3$, and the amplitude is parametrized in a range of $A \in [0, 50]$. The power-law index n is also parametrized in a range of $n \in [0.125, 1]$.

We limit the viscosity to $\mu = \min(\dot{\gamma}^{n-1}, \mu_{\max})$, here μ_{\max} is the maximum viscosity to avoid numerical instability. It is set to $\mu_{\max} = 1 \times 10^4$, which is confirmed to be large enough for the fluid to be regarded as a purely power-law one. The radius of the computational domain is $1 \leq r \leq R_{\max}$, here, the maximum radius is set to $R_{\max} = 1 \times 10^3$. The radial grid width (Δr) increases in geometric progression in the r direction with the minimum $(\Delta r)_{\min} = 1 \times 10^{-2}$. The number of grid points is $N_r \times N_\theta = 128 \times 128$ in the r and θ directions. The time increment is fixed at $\Delta t = 2\pi/(2^{10}\omega)$, which is confirmed to be small enough to capture the unsteady behaviours. Following Sugiyama & Takemura (2010), we employ a numerical method that uses the exact values of the grid width, the cell interfacial area and the control volume in spherical coordinates, and also guarantees the conservation law in a discretized equation. We performed convergence tests of the total energy dissipation rate \dot{E}_{diss} , which is determined from the numerical integral of $\dot{\gamma}^{n+1}$ over the entire computational domain. We confirmed the grid convergence behaviours with decreasing $(\Delta r)_{\min}$ and with increasing $N_r (= N_\theta)$. We also confirmed the energy balance relation that the time-averaged \dot{E}_{diss} is in good agreement with the time-averaged energy input corresponding to FU , where F is numerically evaluated on the bubble wall. Further, we verified the Bobyleff–Forsythe formula (which will be discussed in § 3.3), involving the surface integral of the enstrophy and the volume integrals of the enstrophy and the strain rate square, holds exactly. The accuracy assessment indicates that the simulated results

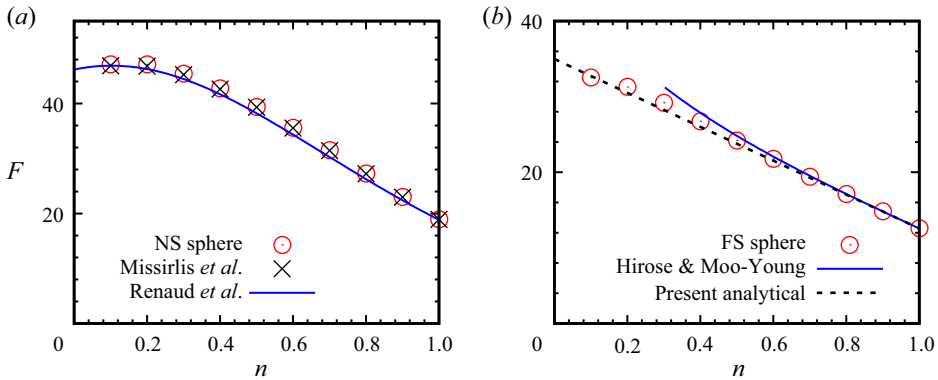


Figure 2. The force F vs the power-law index n for steady creeping flow. The circle symbols indicate the present numerical results. (a) For the NS sphere, the solid curves and the cross symbols indicate the empirical expression (2.11) and the numerical results of Missirlis *et al.* (2001), respectively. (b) For the spherical bubble, the solid and dashed curves indicate the semi-analytical expressions (2.12) and (A14) for $0 < 1 - n \ll 1$.

using the present computational mesh are accurate enough for the subsequent discussion of surface and bulk quantities.

2.3. Validation tests

Validation simulations of fluid flow induced by a sphere travelling in a shear-thinning fluid with no oscillation ($U = 1$) have been conducted. Firstly, we check the validity for a no-slip (NS) sphere since there are several available data in the literature. For the NS sphere, the boundary condition (2.8a,b) is replaced by $\mathbf{u} = \mathbf{e}_x U$. Figure 2 shows the relation between the drag force F and the power-law index n . In figure 2(a) for the NS sphere, the circle symbols and the solid curve respectively indicate the present numerical results and an empirical expression (Renaud *et al.* 2004), corresponding to

$$F = 4\pi \left(\frac{3\sqrt{6}}{2(n^2 + n + 1)} \right)^{n+1}. \quad (2.11)$$

Note that (2.11) was formulated in such a way as to take the analytical value 6π for the Newtonian case ($n = 1$) and to comprehensively capture the variation for any shear-thinning power-law fluid ($0 < n < 1$). The present results are in good agreement with the empirical curve (2.11) over the entire range of n . However, a slight discrepancy is found upon more careful inspection. The cause would be the imperfect accuracy of the empirical expression (2.11). The cross symbols in figure 2(a) indicate the well-validated data of direct numerical simulations (Missirlis *et al.* 2001). These are supposed to be more accurate than (2.11). The present results are in exact agreement with the data from the simulation (Missirlis *et al.* 2001), and we can assert that the discrepancy between the present numerical results and the result predicted by (2.11) is attributed to the underestimation of (2.11). Thus, the present numerical method can reasonably treat the shear-thinning power-law viscosity and solve the equations of the steady creeping flow around the NS sphere.

Secondly, let us determine the spherical bubble's validation in a steady creeping flow. Since such studies are significantly fewer than those of the NS sphere, accessible reference

data are limited in the literature. In [figure 2\(b\)](#) for the spherical bubble, the circle symbols and the solid curve respectively indicate the present results and a semi-analytical expression ([Hirose & Moo-Young 1969](#)), corresponding to

$$F = \frac{4\pi 3^{(n-1)/2}(13 + 4n - 8n^2)}{(2n + 1)(n + 2)}, \tag{2.12}$$

which was derived under the assumption that the deviation from Newtonian flow is small (namely the power-law index n is close to unity (i.e. $0 < 1 - n \ll 1$)), and gives exact value 4π for the Newtonian fluid case $n = 1$. Reconsidering this assumption, we also derive another expression ([A14](#)) in a straightforward way (see [Appendix A](#)). It is drawn in the dashed curve in [figure 2\(b\)](#). For $n \approx 1$ where the precondition in the analyses ([Hirose & Moo-Young 1969](#)) and [Appendix A](#) is fulfilled, the present results are in good agreement with the curves (2.12) and ([A14](#)). Thus, the present numerical method can reasonably treat the power-law viscosity and the FS condition in steady creeping flows. Note that, although the validity of both the expressions (2.12) and ([A14](#)) may be violated for small n , [figure 2\(b\)](#) exhibits the consistency between the present semi-analytical expression ([A14](#)) and numerical results for $n \approx 1$, and also the incidental consistency over a wider range of n .

We have also assessed the present numerical method to predict flows induced by an oscillating spherical bubble in a Newtonian fluid (with the index of $n = 1$). For the bubble velocity $U = \cos \omega t$, the angular frequency was parametrized in a range of $10^{-1} \leq \omega \leq 10^3$. For all the conditions of ω , the numerical results of the temporal change in the force F were confirmed to be in excellent agreement with the analytical solution ([Yang & Leal 1991](#))

$$F = Re \left\{ \left(\frac{2\pi}{3} i\omega + \frac{4\pi (1 + (i\omega)^{1/2})}{1 + \frac{1}{3}(i\omega)^{1/2}} \right) \exp(i\omega t) \right\}. \tag{2.13}$$

The respective effects of the shear-thinning fluid and the oscillation have been validated. The results of numerical simulations by combining these effects will be presented in [§ 3](#).

3. Simulation results

3.1. Velocity and viscosity distribution around the bubble

To overview how the fluid flow is induced owing to the interplay between n and A , the time-averaged velocity and viscosity distribution are investigated. In consideration of the facts that the system is axisymmetric and the radial velocity component u_r is expanded in a Legendre polynomial series, we focus on the radial profile of the first mode $\langle \hat{u}_r \rangle$:

$$\langle \hat{u}_r \rangle(r) = \frac{3}{2} \left\langle \int_0^\pi u_r(r, \theta, t) \cos \theta \sin \theta \, d\theta \right\rangle, \tag{3.1}$$

where $\langle \dots \rangle (= \omega(2\pi)^{-1} \int_0^{2\pi/\omega} \dots dt)$ stands for the time average over one cycle. [Figure 3](#) shows the simulated results of $\langle \hat{u}_r \rangle$ as a function of r . For comparison, two analytical curves ($\langle \hat{u}_r \rangle = r^{-3}$ for the potential flow and $\langle \hat{u}_r \rangle = r^{-1}$ for the Newtonian Stokes flow) with no oscillation $A = 0$ are included therein.

For $n = 1$ ([figure 3d](#)), corresponding to the Newtonian fluid, the plots of $\langle \hat{u}_r \rangle$ collapse onto the monopole curve r^{-1} irrespective of the oscillation amplitude A . This is a natural consequence of the system linearity involved in the Newtonian Stokes equation. The time-average process offsets the oscillation effect. For $0 < n < 1$ ([figure 3a-c](#)),

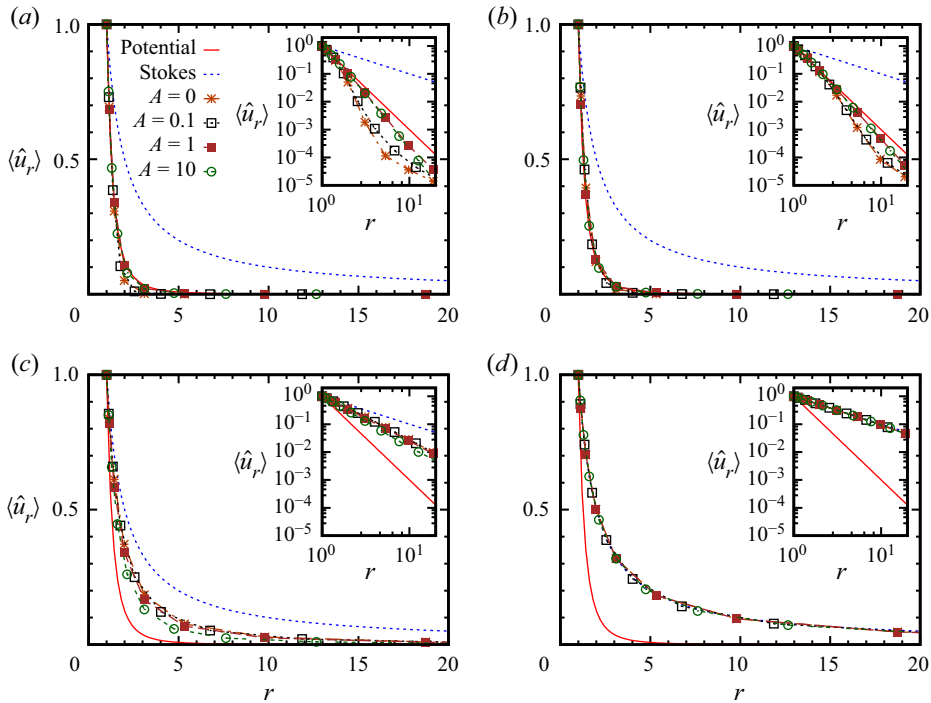


Figure 3. The relation of the time-averaged velocity coefficient $\langle \hat{u}_r \rangle$ as a function of r in the fully developed state for various power-law indices n and oscillation amplitudes A . The solid and dashed curves indicate $\langle \hat{u}_r \rangle = r^{-3}$ for the potential flow and $\langle \hat{u}_r \rangle = r^{-1}$ for the steady Newtonian Stokes flow, respectively. The symbols correspond to the simulated results, where the r positions for the conditions ($A = 0, 0.1, 1, 10$) specified by the symbol types are separated to make the respective profiles comprehensible. The inset shows the log-log plot to clarify the curve slope; (a) $n = 0.125$, (b) $n = 0.25$, (c) $n = 0.75$ and (d) $n = 1$.

corresponding to the shear-thinning fluid, the slope of the profile $\langle \hat{u}_r \rangle$ is steeper with decreasing power-law index n . The viscosity distribution, depending upon the spatial variation of the shear rate, is reflected in such an n -dependent decaying behaviour. For $A = 0$, the slope at $n = 0.75$ (figure 3c) is between -1 (the Newtonian Stokes flow) and -3 (the potential flow), while the profiles at the sufficiently small indices $n = 0.125$ (figure 3a) and $n = 0.25$ (figure 3b) decay more rapidly than the potential flow one. For each n condition, the profiles with varying A are non-monotonic because the nonlinear viscosity to the shear rate is affected by the oscillation amplitude A . Therefore, the bubble oscillation alters the time-averaged viscosity and stress distributions. Carefully observing figure 3(a–c), one finds that, with increasing A , the profile becomes closer to that of the potential flow, implying that the time-averaged vorticity is attenuated in the bulk. At each instant, the vorticity generated on the bubble surface ($r = 1$) is $2\{u_\theta + (1 + A \cos \omega t) \sin \theta\}$ due to the FS condition (Ryskin & Leal 1984), and thus its magnitude is likely to be larger with increasing A . However, it is evident from figure 3(a–c) that the large amplitude oscillation (with the large A) of the bubble in the strong shear-thinning fluid (with the small power-law index n) confines the enhanced vorticity near the bubble wall and hinders the vorticity transfer to the bulk.

For steady flows, the interplay between the spatially non-uniform viscosity and the motion of dispersion (i.e. a bubble, drop or particle) has been investigated by several researchers (e.g. Ohta *et al.* 2005; Zhang, Yang & Mao 2010; Zare, Daneshi & Frigaard

Drag force on an oscillatory spherical bubble

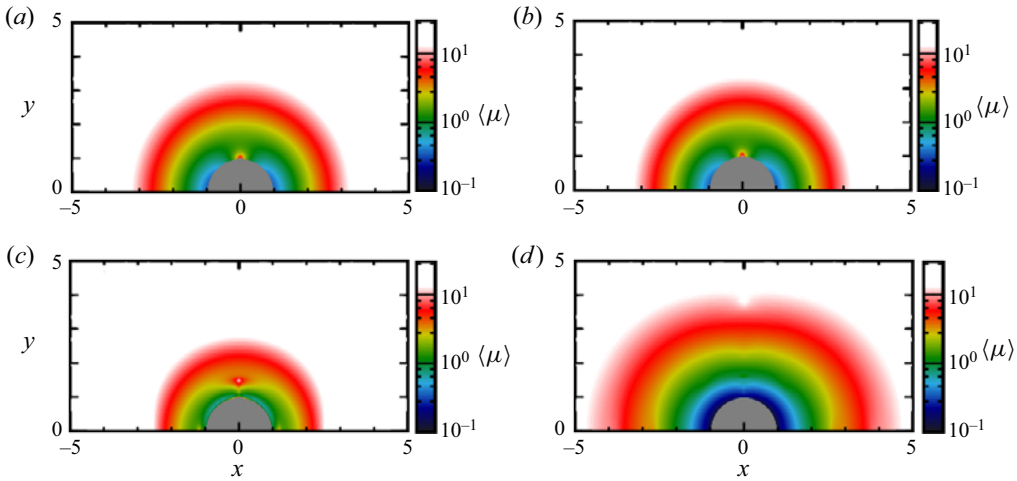


Figure 4. The time-averaged viscosity distribution around the bubble in a fully developed state for various amplitudes A at the power-law index of $n = 0.25$; (a) $A = 0$, (b) $A = 0.1$, (c) $A = 1$ and (d) $A = 10$.

2021). Following the earlier studies, to demonstrate the effect of the oscillation amplitude A on the shear-thinning viscosity, figure 4 visualizes the distribution of the time-averaged viscosity $\langle \mu \rangle$ around the bubble at $n = 0.25$. The colour map exhibits that, for $A \lesssim 1$, the low viscosity region becomes smaller with increasing A , while it becomes larger for $A \gtrsim 1$. A simple rough relation may account for a non-monotonic volume change in the low viscosity region. Under the assumption that the shear rate scales linearly to the bubble velocity magnitude $|U|$, namely $\dot{\gamma} \sim |1 + A \cos \omega t|/\ell$ (here, the length scale ℓ is hypothetically fixed), the instantaneous viscosity scales as $\mu \sim |1 + A \cos \omega t|^{n-1}$. With this relation, for a sufficiently small amplitude $0 < A \ll 1$, the time-averaged viscosity may scale as $\langle \mu \rangle \sim 1 + (1 - n)(2 - n)A^2/4$, which increases with A as long as $0 < n < 1$, while for the sufficiently large amplitude $A \gg 1$, it may scale as $\langle \mu \rangle \sim A^{n-1}$, which decreases with A . Therefore, $\langle \mu \rangle$ is inferred to be maximized at a moderate A . The high viscosity region (corresponding to the non-coloured area in figure 4) is the largest at the moderate amplitude $A = 1$. Note that, even though the non-monotonic behaviour of the shear-thinning viscosity with varying A is explainable in terms of the bubble velocity, unlike a steady flow, the time-averaged viscosity $\langle \mu \rangle$ in the unsteady flow is not necessarily correlated with the time-averaged force $\langle F \rangle$. It is because the time-averaged viscous stress, which is given by $\langle \boldsymbol{\tau} \rangle = \langle 2\mu \mathbf{S} \rangle \neq 2\langle \mu \rangle \langle \mathbf{S} \rangle$, is not proportional to $\langle \mu \rangle$. To discuss the time-averaged force on the bubble in a strong shear-thinning fluid, we will consider a nearly irrotational velocity field with a large amplitude oscillation (figure 3a,b). Further, we will examine the overall energy balance in the unsteady fluid motion rather than the viscosity distribution.

3.2. The effect of the oscillation amplitude A on the force acting on the bubble

Figure 5 shows the temporal change in the force F at the power-law index of $n = 0.25$ and its velocity $U (= 1 + A \cos \omega t)$ for various oscillation amplitudes A . Here, we shall separately discuss the fluctuating and time-averaged components of F . Firstly, on the fluctuating force, we confirm that the amplitude of F is approximated by $2\pi\omega A/3$ and the phase difference between F and U is approximately $\pi/2$. These features imply that the

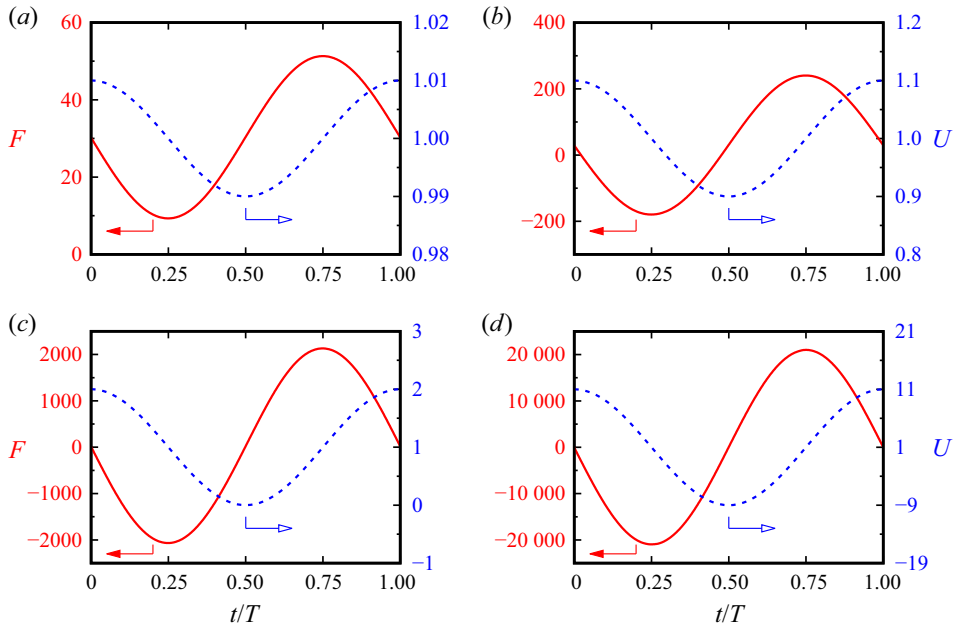


Figure 5. Temporal change in the force F on the bubble (solid curve) and its velocity $U (= 1 + A \cos \omega t)$ (dashed curve) for one cycle in the fully developed state for various oscillation amplitudes A at the power-law index of $n = 0.25$. The horizontal axis is in scaled time t/T , and here $T (= 2\pi/\omega)$ is the period; (a) $A = 0.01$, (b) $A = 0.1$, (c) $A = 1$ and (d) $A = 10$.

fluctuating component of F is consistent with the added inertia force $-(2\pi\omega A/3) \sin \omega t$ on a translationally oscillating sphere, indicating that the potential flow well describes the fluctuating velocity distribution at each instant. In Newtonian fluid flows, as indicated in (2.13) with a conversion of $\omega \Rightarrow \omega A$, such a potential approximation is valid for sufficiently high frequency $\omega \gg 1$. This is because the amplitude of the added inertia force (corresponding to the first term inside the curly brackets in (2.13)) is proportional to ωA and is much greater than that of the history force (corresponding to the second term), likely to be proportional to $(\omega A)^\beta$ with $\beta \leq 1/2$. This relation of the added inertia force would also hold for the non-Newtonian power-law fluid flow at $\omega = 1 \times 10^3 \gg 1$ in the present study. Since the added inertia force is expressed as a temporally sinusoidal function proportional to $\sin \omega t$, it makes no contribution to the time-averaged component.

Secondly, we pay attention to the time-averaged drag force denoted by $D (= \langle F \rangle)$. Figure 6(a) shows the relation between D and A . When the amplitude A is sufficiently smaller than unity, the drag force D approaches that with no oscillation D_0 . For $A \gtrsim 1$, D substantially decreases with increasing A . This result implies that the shear-thinning effect, enhanced with A , causes the drag reduction. This is unlike the fluctuating component of the force F , for which the amplitude increases with A (figure 5) owing to the added inertia force. To highlight the deviation of the time-averaged drag force with oscillation D from that with no oscillation D_0 , figure 6(b) depicts the drag reduction ratio ($DDR (= 1 - D/D_0)$) as a function of the oscillation amplitude A . For $A \lesssim 1$, DDR is likely to be proportional to A^2 , while for $A \gtrsim 1$, DDR is saturated to 1 (corresponding to the upper bound as long as $D > 0$) with increasing A . The proportionality of $DDR \propto A^2$ rather than A^1 for sufficiently small A comes from the nonlinearity in the power-law viscosity and is explained from the idea of the weakly nonlinear perturbation method.

Drag force on an oscillatory spherical bubble

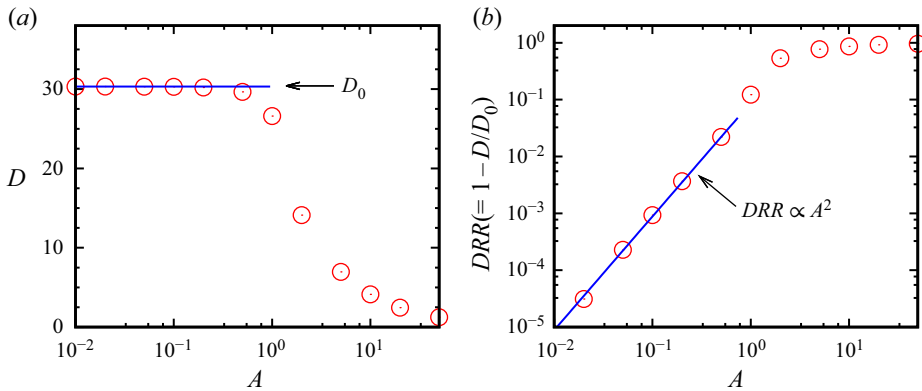


Figure 6. The relationship between time-averaged drag force D and oscillation amplitude A at the power-law index of $n = 0.25$. The circle symbols indicate the simulated results. Here, $D_0 (= 30.32)$ is the drag force with no oscillation ($A = 0$). Panel (a) shows D vs A . The solid curve represents D_0 . Panel (b) shows a log–log plot of the drag reduction ratio ($DRR (= 1 - D/D_0)$) vs A . The solid line corresponds to a curve with a slope of 2, namely $DRR \propto A^2$.

Assuming $0 < A \ll 1$, which is chosen as a perturbation, we write the time-dependent force in a series form as $F = D_0 + \alpha_1 A^1 + \alpha_2 A^2 + \dots$ for each n (here, $\alpha_1 = \alpha_1(t)$ and $\alpha_2 = \alpha_2(t)$ are time-dependent functions). In the present system, the $O(A^1)$ contribution has the time dependence on $\cos \omega t$ and/or $\sin \omega t$. Hence, the time-averaged value thereof vanishes (i.e. $\langle \alpha_1 \rangle = 0$). In contrast, the $O(A^2)$ contribution comes from the correlation between the $O(A^1)$ variations in the viscosity and the strain rate. It involves the time dependence of $\cos^2 \omega t$ and/or $\sin^2 \omega t$. Hence, the time-averaged value thereof is non-zero (i.e. $\langle \alpha_2 \rangle \neq 0$), and the second-order approximation of the time-averaged drag force is expressed as $D = D_0 + \langle \alpha_2 \rangle A^2$, accounting for the relation of $1 - D/D_0 \propto A^2$, as seen for $A \lesssim 1$ in figure 6(b). Note that Phan-Thien & Dudek (1982b) demonstrated a similar mechanism of the second-order drag reduction in pulsating pipe flows of a polymeric fluid owing to the viscosity’s nonlinearity.

For sufficiently large A , the saturation of $1 - D/D_0 \approx 1$ in figure 6(b) indicates that the time-averaged drag force becomes small enough ($D \ll D_0$). To highlight how such an intense drag reduction depends upon the power-law index n , figure 7 depicts the drag reduction behaviour for various n : the log–log plot of the time-averaged scaled drag force D/D_0 vs A (figure 7a) and the slope $d(\log D)/d(\log A)$ vs A (figure 7b). In figure 7(a), the simulated results for $A \gtrsim 1$ exhibit a constant slope in the decaying profile for each n . The solid lines indicate the fitted curves proportional to A^{n-1} , which capture the simulated results for the respective n as long as the amplitude A is large enough. Figure 7(b) corresponds to the slopes of the curves in figure 7(a), indicating the shear-thinning effect for each n . The fluid with a smaller power-law index n has the stronger shear-thinning effect and the scaled drag force on the bubble in it is more significantly reduced, corresponding to the same amplitude of oscillation. Note that a similar power law in the drag reduction was found for a radially oscillating bubble rising in a shear-thinning fluid (De Corato *et al.* 2019a). De Corato *et al.* (2019a) could separately treat the radial and translational motions of the bubble with two velocity scales \dot{R} and U . The viscosity distribution affected by \dot{R} was assumed to be spherically symmetric. In contrast, we cannot separately treat the effect of the constant and oscillatory velocities of the bubble. Thus, in the present study, the shear-thinning viscosity is affected by both motions, and its distribution is

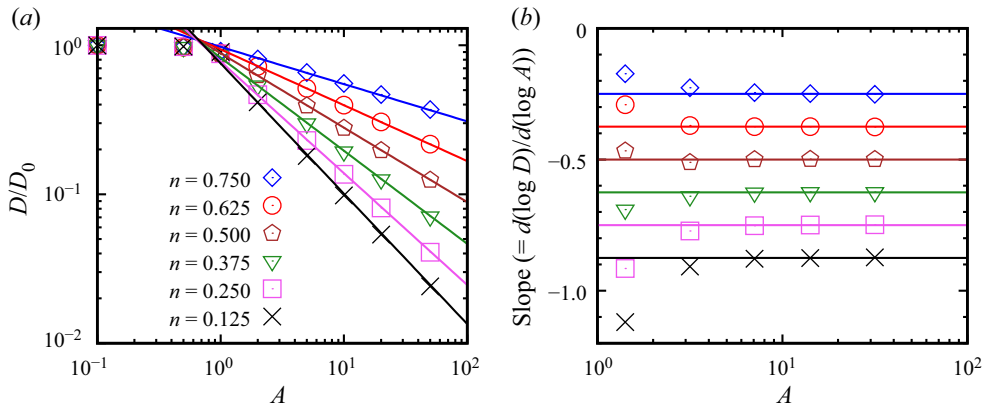


Figure 7. The relation between the time-averaged scaled drag force D/D_0 and the oscillation amplitude A for various power-law indices n . The symbols represent the simulated results with the respective power-law index n specified in the panel. Panel (a) shows D/D_0 vs A . The solid curve for each n indicates the curve proportional to A^{n-1} . Panel (b) shows $d(\log D)/d(\log A)$ vs A , corresponding to the slope in (a). The solid curve for each n indicates the value of $n - 1$.

not spherically symmetric. Subsequently, we will discuss the drag reduction mechanism resulting in the expression of $D/D_0 \propto A^{n-1}$.

3.3. Discussion of the drag reduction mechanism

We now investigate how the vorticity is generated on the bubble wall, is distributed over the space and affects the force due to the interplay between the FS boundary condition and the high frequency. Before examining the non-Newtonian fluid flow, we shall recall the Newtonian one, including a sphere with a velocity of $U = 1 + A \cos \omega t$. On a NS sphere, the force F_{NS} is written in a form (Landau & Lifschitz 1987)

$$F_{NS} = 6\pi + Re \left\{ A \left(\frac{2\pi}{3} i\omega + 6\pi(i\omega)^{1/2} + 6\pi \right) \exp(i\omega t) \right\}, \quad (3.2)$$

where the first and second terms on the right-hand side are the steady drag force associated with the constant unity velocity and the force with oscillatory velocity $A \cos \omega t$, respectively. In (3.2), the first, second and third terms inside the parentheses before $\exp(i\omega t)$ indicate the added inertia force, the Basset history force and the drag force, respectively. On a spherical bubble (referred to as a FS sphere), the general expression of the force F_{FS} for arbitrary angular frequencies ω is given by the combination of 4π (associated with the constant unity velocity) and (2.13) multiplied by the amplitude A (associated with $A \cos \omega t$). At sufficiently high frequencies ($\omega \gg 1$), F_{FS} is simplified into

$$F_{FS} = 4\pi + Re \left\{ A \left(\frac{2\pi}{3} i\omega + 12\pi + O(\omega^{-1/2}) \right) \exp(i\omega t) \right\}. \quad (3.3)$$

In (3.3), the first and second terms inside the parentheses before $\exp(i\omega t)$ indicate the added inertia and Levich drag forces, respectively (Magnaudet & Eames 2000; Liu, Sugiyama & Takagi 2016). The term of order $\omega^{-1/2}$ vanishes when $\omega \gg 1$. Here, we pay attention to the temporally oscillatory force, i.e. the second term in (3.2) and (3.3). At high frequencies, for the NS sphere, the penetration depth ℓ of the rotational flow is of the order $\omega^{-1/2}$ (Landau & Lifschitz 1987), and hence the magnitude of the vorticity

Drag force on an oscillatory spherical bubble

generated on the sphere wall scales as $\ell^{-1} \sim \omega^{1/2}$. By contrast, for the bubble, the vorticity magnitude scales as ω^0 owing to the FS condition (Ryskin & Leal 1984). The difference in the order of the generated vorticity magnitude is reflected in the presence (3.2) or absence (3.3) of the $O(\omega^{1/2})$ term in the force expression. Note that, for the bubble, the temporally oscillatory force (corresponding to the second term in (3.3)) is consistent with the force in a viscous potential flow (Joseph 2006), which is irrotational but involves the viscous dissipation mechanism, even though it is derived in the low Reynolds number limit. Such a consistent expression is justified as long as the vorticity magnitude in the bulk is negligible. Although this feature is reflected in the force expression (3.3) for the Newtonian creeping flow, the mechanism of the negligible bulk vorticity would be explained by that the interplay between the FS condition and the high frequency hinders the vorticity diffusion irrespective of Newtonian or non-Newtonian fluid.

Again, we will see the simulation results. Quantifying the level of bulk vorticity, we will discuss the applicability of the potential flow theory to the non-Newtonian power-law fluid. To this end, we employ the Bobileff–Forsythe (BF) formula (Serrin 1959; Kang & Leal 1988; Stone 1993) for any velocity field \mathbf{v} satisfying the solenoidal condition ($\nabla \cdot \mathbf{v} = 0$) and the kinematic and FS boundary conditions (2.8a,b), which are expressed as

$$\beta_1(\mathbf{v}) = \beta_2(\mathbf{v}) + \beta_3(\mathbf{v}), \quad (3.4)$$

where

$$\left. \begin{aligned} \beta_1(\mathbf{v}) &= \frac{1}{2} \int_V (\nabla \mathbf{v} + (\nabla \mathbf{v})^T) : (\nabla \mathbf{v} + (\nabla \mathbf{v})^T) dV, \\ \beta_2(\mathbf{v}) &= \int_V \boldsymbol{\omega} \cdot \boldsymbol{\omega} dV, \quad \beta_3(\mathbf{v}) = \frac{1}{2} \oint_{r=1} \boldsymbol{\omega} \cdot \boldsymbol{\omega} dS, \end{aligned} \right\} \quad (3.5)$$

and $\boldsymbol{\omega} = \nabla \times \mathbf{v}$ is the vorticity. Note that $\beta_k \geq 0$ for $k = 1, 2$ and 3 . The BF formula (3.4) characterizes the contributions of the bulk enstrophy β_2 and the surface one β_3 to the overall strain rate square β_1 . We will apply it to the present simulation results of (i) the instantaneous velocity (by choosing $\mathbf{v} = \mathbf{u}$) and (ii) the time-averaged one (by $\mathbf{v} = \langle \mathbf{u} \rangle$).

Firstly, for the instantaneous velocity, figure 8 shows the temporal change in $\beta_1(\mathbf{u})$, $\beta_2(\mathbf{u})$ and $\beta_3(\mathbf{u})$ parametrizing oscillation amplitudes A at the small power-law index of $n = 0.25$. The contribution of the surface enstrophy β_3 to the overall strain rate square β_1 becomes more prominent with increasing A . For $A \gtrsim 1$, β_3 is almost in balance with β_1 , while the bulk enstrophy β_2 is negligibly smaller than β_1 and β_3 . This result indicates that, at sufficiently large amplitudes, the vorticity generated on the FS boundary is confined to the vicinity of the bubble wall, and the bulk flow may be regarded as nearly irrotational. Such an irrotational nature at each instant rationalizes the result of figure 5 that the added inertia force of the potential flow well describes the fluctuating component of the force F .

Secondly, for the time-averaged velocity $\langle \mathbf{u} \rangle$, figure 9 shows $\beta_1(\langle \mathbf{u} \rangle)$, $\beta_2(\langle \mathbf{u} \rangle)$ and $\beta_3(\langle \mathbf{u} \rangle)$ as a function of the oscillation amplitude A for various power-law indices n . All the panels include the potential flow solution ($\beta_1 = \beta_3 = 12\pi$; see (B2a–c) in Appendix B) for comparison. For the Newtonian fluid with $n = 1$ (figure 9d), $\beta_1(\langle \mathbf{u} \rangle)$, $\beta_2(\langle \mathbf{u} \rangle)$ and $\beta_3(\langle \mathbf{u} \rangle)$ are constant independent of A , and equal to the analytical solutions 4π , $8\pi/3$ and $4\pi/3$, respectively, for the steady Newtonian Stokes flow (see (B4a–c) in Appendix B). This is a natural consequence because the time-averaged velocity satisfies the steady Stokes equation, and is the same as the steady flow one owing to the system linearity. For shear-thinning fluids with $0 < n < 1$, the time-averaged velocity $\langle \mathbf{u} \rangle$ is not proportional to the time-averaged speed of the bubble $\langle U \rangle = \langle 1 + A \cos \omega t \rangle = 1$. It depends upon the

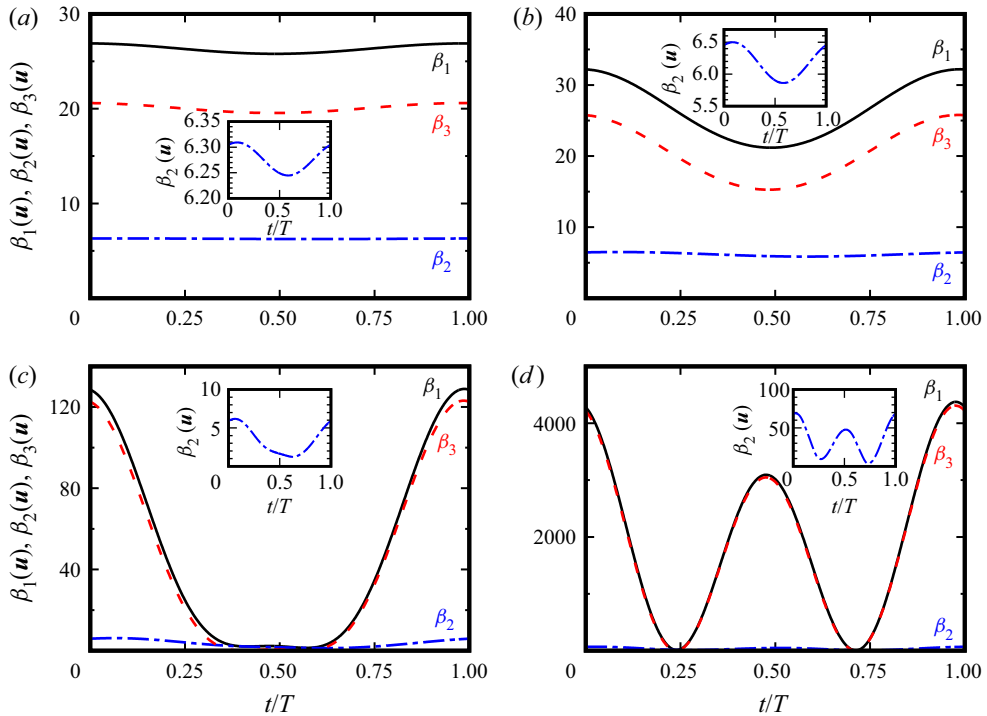


Figure 8. Temporal change in $\beta_1(u)$, $\beta_2(u)$ and $\beta_3(u)$ (for the instantaneous velocity u) at the power-law index of $n = 0.25$. The solid and dashed curves indicate β_1 and β_3 , respectively. The dash-dotted curve indicates β_2 ; (a) $A = 0.01$, (b) $A = 0.1$, (c) $A = 1$ and (d) $A = 10$.

oscillation amplitude A owing to the system nonlinearity. Therefore, as in figure 9(a–c), β_1 , β_2 and β_3 are no longer constant with respect to A . For smaller amplitudes $A < 1$, the surface entrophy contribution β_3 increases with A , and the bulk one β_2 reduces, while for larger amplitude $A > 1$, both β_2 and β_3 are rather independent of A . In the case of the strongly shear-thinning fluids with the small power-law indices $n = 0.125$ (figure 9a) and $n = 0.25$ (figure 9b), for $A > 1$, the reduced contribution of the bulk entrophy β_2 becomes sufficiently smaller than the overall strain rate square β_1 . The increased contribution of the surface entrophy (β_3 for $A > 1$) is almost in balance with β_1 . This result implies that the interplay between the small index n and the large amplitude A confines the time-averaged vorticity $\nabla \times \langle u \rangle$ near the bubble wall and attenuates it in the bulk. This is consistent with the results of figure 3(a,b) that the velocity field is regarded as nearly irrotational at large amplitudes A . Although the reduction in the bulk entrophy is attributed to the system nonlinearity, it is non-trivial to explain the cause. A possible mechanism could be that, unlike the Newtonian Stokes flow, in which the effect of the oscillatory velocity $A \cos \omega t$ on any time-averaged quantity is compensated to be zero, the breaking symmetry in the vastly fluctuating velocity about the non-zero time-averaged speed of the bubble $\langle U \rangle = 1$ alters the time-averaged quantities, and would reduce the bulk vorticity owing to the nearly irrotational fluid motion at each instant with large A (as in figure 8c,d). In consideration that the instantaneous (figure 8) and time-averaged (figure 9) entropies in the bulk are small enough with small index n and large amplitude A , we will examine the energy balance with the help of the potential flow theory (Chhabra 1998).

Drag force on an oscillatory spherical bubble

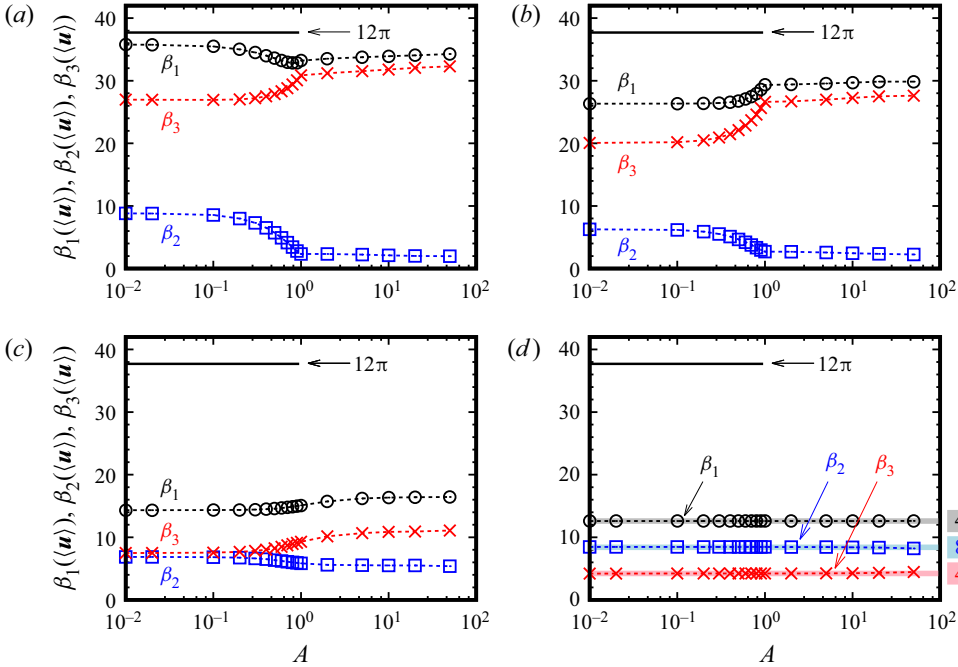


Figure 9. Values of $\beta_1(\mathbf{u})$, $\beta_2(\mathbf{u})$ and $\beta_3(\mathbf{u})$ vs the oscillation amplitude A (for the time-averaged velocity \mathbf{u}). The circle, square and cross symbols indicate β_1 , β_2 and β_3 , respectively; (a) $n = 0.125$, (b) $n = 0.25$, (c) $n = 0.75$ and (d) $n = 1$ (corresponding to the Newtonian fluid). The solid lines marked by 4π , $8\pi/3$ and $4\pi/3$ in (d) respectively indicate the analytical solutions of β_1 , β_2 and β_3 for a steady Newtonian Stokes fluid.

In an irrotational flow, substituting each component of the strain rate tensor \mathbf{S} (in (B1)) into (2.7a,b) gives the shear rate $\dot{\gamma}$:

$$\dot{\gamma} = \frac{3|U|}{r^4} \sqrt{1 + 2 \cos^2 \theta}. \tag{3.6}$$

Let ε be the energy dissipation rate. For power-law fluids, it is written as

$$\varepsilon = 2\mu \mathbf{S} : \mathbf{S} = \dot{\gamma}^{n+1}. \tag{3.7}$$

Let \dot{E}_{diss} be the total rate of energy dissipation, which is defined as the volume integral of ε over the entire fluid region. From (2.3), (3.6) and (3.7), \dot{E}_{diss} in the irrotational motion of the power-law fluid is

$$\dot{E}_{diss} = 2\pi \int_0^\pi \int_1^\infty \varepsilon r^2 \sin \theta \, dr \, d\theta = \frac{4\pi 3^{n+1} \lambda(n)}{4n + 1} |1 + A \cos \omega t|^{n+1}, \tag{3.8}$$

where

$$\lambda(n) = \frac{1}{2} \int_{-1}^1 (1 + 2\zeta^2)^{(n+1)/2} \, d\zeta. \tag{3.9}$$

For the approximated expression of $\lambda(n)$, see (C2) in Appendix C. To assess the potential flow model (3.8), figure 10 shows the total energy dissipation rate \dot{E}_{diss} in one cycle for various amplitudes A at $n = 0.25$. Overall, the theoretical prediction (3.8) well captures the temporal fluctuation of \dot{E}_{diss} of the simulated results. For smaller amplitudes $A \ll 1$

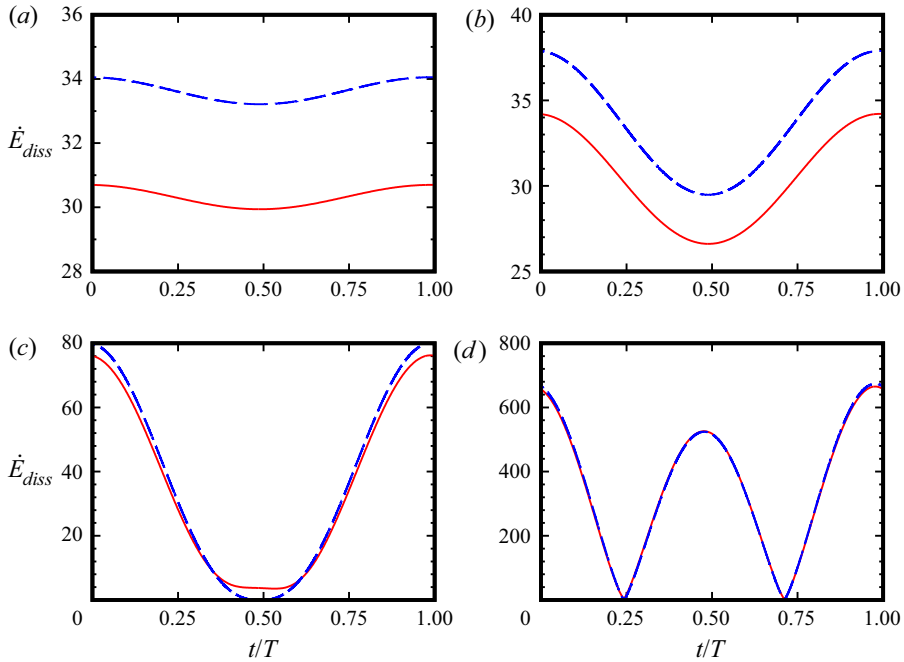


Figure 10. Temporal change in the total energy dissipation rate \dot{E}_{diss} at the power-law index of $n = 0.25$. The solid and dashed curves indicate the simulated result and the prediction (3.8) based on potential flow theory, respectively; (a) $A = 0.01$, (b) $A = 0.1$, (c) $A = 1$ and (d) $A = 10$.

(figure 10a,b), where the fluctuation level of numerical \dot{E}_{diss} is much smaller than the value of theoretical \dot{E}_{diss} , the theoretical prediction (3.8) overestimates the simulated one. By contrast, for larger amplitude $A \gtrsim 1$ (figure 10c,d), where the fluctuation level is comparable to the theoretical prediction of \dot{E}_{diss} , the relative agreement between the theoretical and simulated predictions become better. Note that figure 10(d) for $A = 10$ exhibits a rectified waveform of $\dot{E}_{diss} > 0$ as indicated by the theoretical prediction (3.8) in the case of $A > 1$.

In the examination of the energy balance, we now pay attention to the total energy input rate $\dot{E}_{in} = FU$ from the bubble to the surrounding fluid. A general expression of the energy balance over one cycle is

$$\langle \dot{E}_{in} \rangle = \langle \dot{E}_{diss} \rangle. \tag{3.10}$$

Applying the theoretical model (3.8) under the assumption of potential flow to (3.10) gives

$$\langle \dot{E}_{in} \rangle = \frac{4\pi 3^{n+1} \lambda(n)}{4n + 1} \langle |1 + A \cos \chi|^{n+1} \rangle_{\chi}, \tag{3.11}$$

where $\langle \dots \rangle_{\chi}$ stands for the average in the range of $\chi \in [0, 2\pi]$. For sufficiently large amplitude A (when the rectified waveform of \dot{E}_{diss} is established as in figure 10 (d)), we obtain the asymptotic expression of (3.11)

$$\langle \dot{E}_{in} \rangle \rightarrow \frac{4\pi 3^{n+1} \lambda(n)}{4n + 1} \langle |\cos \chi|^{n+1} \rangle_{\chi} A^{n+1} \text{ as } A \rightarrow \infty, \tag{3.12}$$

indicating $\langle \dot{E}_{in} \rangle \propto A^{n+1}$ for each n . For the approximated expression of $\langle |\cos \chi|^{n+1} \rangle_{\chi}$, see (C4). Note that, for the Newtonian fluid with $n = 1$, (2.3) and (3.3) give

Drag force on an oscillatory spherical bubble

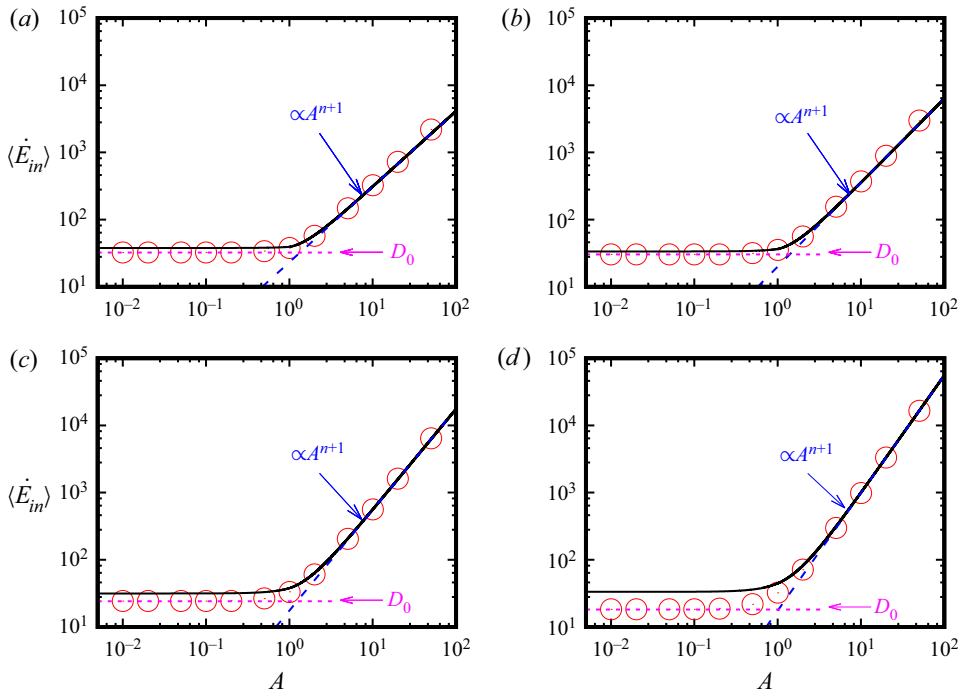


Figure 11. The time-averaged total energy input rate $\langle \dot{E}_{in} \rangle$ vs the oscillation amplitude A for various power-law indices n . The circle symbols indicate the simulated results. The solid and dashed curves indicate the prediction (3.11) based on potential flow theory and its asymptotic expression (3.12) for $A \gg 1$, respectively. The dotted line corresponds to the drag force D_0 without oscillation; (a) $n = 0.125$, (b) $n = 0.25$, (c) $n = 0.5$ and (d) $n = 0.75$.

$\langle \dot{E}_{in} \rangle = 4\pi + 6\pi A^2 \rightarrow 6\pi A^2$ as $A \rightarrow \infty$, consistent with (3.12) at $n = 1$. Figure 11 shows the time-averaged total energy input rate $\langle \dot{E}_{in} \rangle$ as a function of the oscillation amplitude A for various power-law indices n . The simulated results are estimated from $\langle \dot{E}_{in} \rangle = \langle FU \rangle$ using the time-series data of the force F and the bubble velocity U (e.g. those in figure 5). These are compared with the potential flow model (3.11), its asymptotic expression (3.12) for $A \gg 1$, and the drag force D_0 (corresponding to the input rate \dot{E}_{in} in the case of no oscillation ($U = 1$)). For small amplitude $A < 1$, the simulated results of $\langle \dot{E}_{in} \rangle$ at each n approach D_0 with decreasing A . For large amplitude $A \gtrsim 1$, the theoretical predictions (3.11) and (3.12) are in excellent agreement with the simulated results, demonstrating the validity of the proportionality $\langle \dot{E}_{in} \rangle \propto A^{n+1}$ for $A \gg 1$ on the basis of the potential flow theory.

Examining the momentum balance, we shall explain the mechanism of drag reduction shown in figure 7(a). We will address the issue that for $A \gg 1$, the time-averaged drag force $D = \langle F \rangle \propto A^{n-1}$ in the shear-thinning power-law fluid ($0 < n < 1$) is negatively correlated with the amplitude A . This is in contrast to the time-averaged input rate $\langle \dot{E}_{in} \rangle = \langle FU \rangle \propto A^{n+1}$ and the fluctuation level of the bubble velocity $|U| \sim A^1$, which are positively correlated with A , and the time-averaged bubble velocity $\langle U \rangle = 1 \propto A^0$, which is independent of A . We consider the fact that the bubble velocity U determines the kinematics of the irrotational motion at each instant, and the total energy dissipation rate \dot{E}_{diss} with no time lag (3.8). Therefore, in expressing the force F , we neglect history forces (e.g. the Basset force corresponding to the $O(\omega^{1/2})$ term in (3.2)), which are related to

vorticity generation and diffusion. Following the dissipation method (Joseph 2006) for a flow driven by an accelerating sphere, we model the time-dependent force in the form

$$F = \frac{2\pi}{3} \frac{dU}{dt} + \frac{\dot{E}_{diss}}{U}, \tag{3.13}$$

where the first term on the right-hand side corresponds to the added inertia force, which involves the considerable fluctuation in figure 5, and the second term is regarded as the instantaneous drag force. Note that the force decomposition in (3.13) is valid when the system involves the viscous dissipation mechanism with no bulk vorticity. The added inertia force does not influence the time-averaged drag force since it is written in a time-derivative form. Thus, the time-averaged value is zero. Further, it has no impact on the time-averaged total energy input rate $\langle \dot{E}_{in} \rangle = \langle FU \rangle$ because $(2\pi/3)(dU/dt) \times U = (\pi/3)(dU^2/dt)$ is also in a time-derivative form. Therefore, (3.13) satisfies the energy balance $\langle FU \rangle = \langle \dot{E}_{diss} \rangle$ over one cycle (3.10). From (2.3), (3.8) and (3.13) under the assumption of the potential flow, we model the time-averaged drag force

$$D = \left\langle \frac{\dot{E}_{diss}}{U} \right\rangle = \frac{4\pi 3^{n+1} \lambda(n)}{4n + 1} \langle |1 + A \cos \chi|^{n-1} (1 + A \cos \chi) \rangle_{\chi}. \tag{3.14}$$

For sufficiently large amplitude A , (3.14) is asymptotically written in a form

$$D \rightarrow \frac{4\pi 3^{n+1} \lambda(n)}{4n + 1} n \langle |\cos \chi|^{n-1} \rangle_{\chi} A^{n-1} \text{ as } A \rightarrow \infty. \tag{3.15}$$

For the approximated expression of $\langle |\cos \chi|^{n-1} \rangle_{\chi}$, see (C6). The asymptotic expression (3.15) indicates that, although the fluctuation level of the instantaneous drag force scales as $|\dot{E}_{diss}/U| \sim A^n$ for $A \gg 1$, the time-averaged drag force scales as $D \sim A^{n-1}$ owing to the compensation between the positive and negative values of \dot{E}_{diss}/U during one cycle, revealing the fact that the time-averaged drag force D decreases with A in case of the shear-thinning fluid ($0 < n < 1$). Interestingly, the n dependence of this proportionality $D \propto A^{n-1}$ is consistent with the scaling relation of the drag reduction shown in figure 7(a). For more quantitative discussion, figure 12 shows the time-averaged drag force D as a function of the oscillation amplitude A for various power-law indices n . The simulated results are compared with the potential flow model (3.14), its asymptotic expression (3.15) for $A \gg 1$ and the drag force D_0 without oscillation. For small amplitude $A < 1$, the simulated results at each n approach D_0 with decreasing A . For large amplitude $A \gtrsim 1$, as shown in figure 12(c,d), the discrepancy between the model ((3.11) or (3.12)) and simulated predictions becomes more considerable with increasing n since the potential flow assumption is likely to fail as indicated by the gentle slope of the profile $\langle \hat{u}_r \rangle$ in figure 3(c) and the non-negligible bulk enstrophy in figure 9(c). Nevertheless, for all the indices n in figure 12, the slope of D vs A predicted by the asymptotic expression (3.15) for $A \gg 1$ is confirmed to be consistent with the simulated results. For the small indices $n = 0.125$ (figure 12a) and $n = 0.25$ (figure 12b), the model predictions (3.14) and (3.15) are in quantitative agreement with the simulated results for $A \gtrsim 1$.

The mechanism of the drag reduction expressed as $D/D_0 \propto A^{n-1}$ (figure 7a) is explained by the application of the dissipation method (Joseph 2006) to the irrotational flow of the power-law fluid. In particular, for the flow induced by the largely oscillating bubble in the strongly shear-thinning fluid characterized by the small power-law index n , the bulk enstrophy is small enough (figures 8 and 9). Thus, the potential flow assumption becomes reasonable, enabling the model (3.15) thereunder to predict the time-averaged drag force D quantitatively.

Drag force on an oscillatory spherical bubble

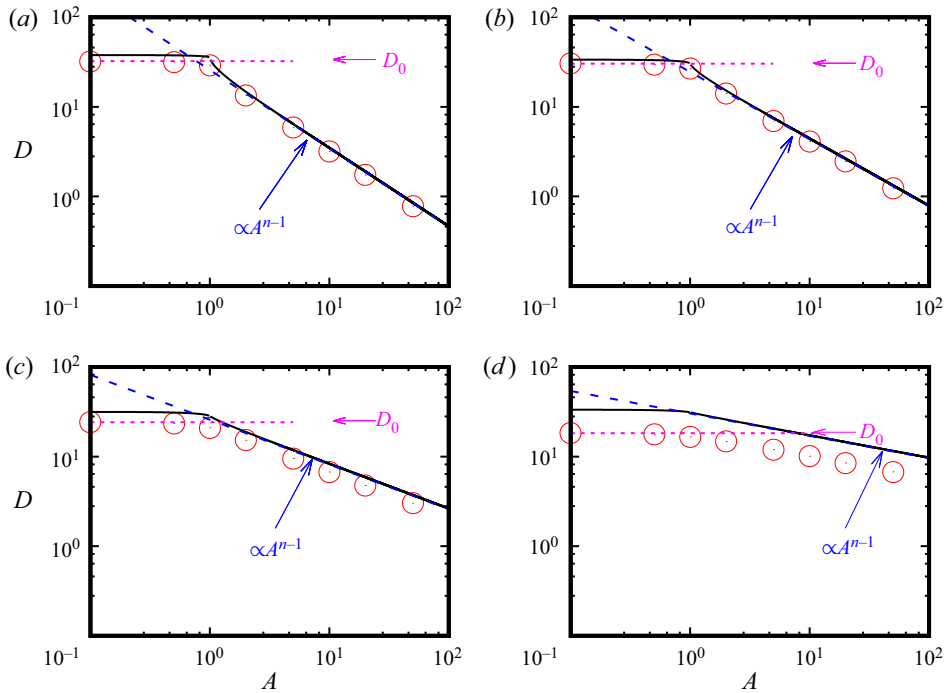


Figure 12. The time-averaged drag force D vs the oscillation amplitude A for various power-law indices n . The circle symbols indicate the simulated results. The solid and dashed curves indicate the prediction (3.14) based on potential flow theory and its asymptotic expression (3.15) for $A \gg 1$, respectively. The dotted line corresponds to the drag force D_0 without oscillation; (a) $n = 0.125$, (b) $n = 0.25$, (c) $n = 0.5$ and (d) $n = 0.75$.

4. Conclusion

In summary, performing numerical simulation and modelling, we have studied the flow dynamics induced by an oscillatory spherical bubble travelling in a power-law shear-thinning fluid with a velocity of $U(= 1 + A \cos \omega t)$. The drag reduction ratio $1 - D/D_0$ is proportional to A^2 at small oscillation amplitude A , and the proportionality of A^2 originates from the fact that the time average of the force contribution proportional to A^1 becomes zero. In contrast, for large amplitude, the drag ratio D/D_0 is proportional to A^{n-1} . In the case of $A \gg 1$, examination of the radial profile of the time-averaged velocity and the level of the bulk enstrophy with the aid of the BF formula revealed that the bulk flow might be regarded as nearly irrotational for a strong shear-thinning fluid with a small power-law index n .

Following the dissipation method (Joseph 2006) for an irrotational flow driven by an accelerating sphere, we developed the potential flow model to describe the total energy dissipation rate at each instant and the time-averaged drag force D . The model quantitatively captures the numerical results of the energy and momentum balance relations, especially at large A and small n . It also accounts for the mechanism of the drag reduction given by the power-law relation $D/D_0 \propto A^{n-1}$.

Our findings have potentially significant implications for applying mechanical oscillation in engineering fields to predict the drag force and to control a bubble's behaviour. Although the present study treated a simple system (i.e. unsteady incompressible creeping flow with a spherical bubble moving at a prescribed speed in a

power-law fluid), it provided a fundamental perspective on the drag reduction mechanism that would boost future research on more complex systems involving e.g. a more general shear-thinning viscosity, a wider variation in frequency, advective momentum transport, liquid compressibility and an acoustic boundary layer.

Acknowledgements. X.Z. acknowledges the Junior Research Associate Program in RIKEN, and thanks Professor H. Yokota and Mr S. Noda for encouraging the present study. Part of the simulation was performed on a supercomputing system HOKUSAI Great Wave and Big Waterfall at the Information Systems Division, RIKEN.

Declaration of interests. The authors report no conflict of interest.

Author ORCIDs.

① Xianping Zhang <https://orcid.org/0000-0001-7897-492X>;

① Tomoaki Watamura <https://orcid.org/0000-0002-4217-7109>.

Appendix A. Drag force on a spherical bubble in a steady flow with a power-law index n close to unity

We define a small parameter as $\epsilon = 1 - n$, which is supposed to be $0 < \epsilon \ll 1$. Based on the method of perturbation, we write the velocity, pressure and viscous stress in an expansion form:

$$\left. \begin{aligned} \mathbf{u} &= \mathbf{u}^{(0)} + \epsilon \mathbf{u}^{(\epsilon)}, \\ p &= p^{(0)} + \epsilon p^{(\epsilon)}, \\ \boldsymbol{\tau} &= \boldsymbol{\tau}^{(0)} + \epsilon \boldsymbol{\tau}^{(\epsilon)}. \end{aligned} \right\} \quad (\text{A1})$$

Applying the Taylor expansion to the viscosity μ with respect to ϵ gives

$$\mu = \dot{\gamma}^{-\epsilon} = \mu^{(0)} + \epsilon \mu^{(\epsilon)} \dots, \quad (\text{A2})$$

where the leading and perturbed components $\mu^{(0)}$ and $\mu^{(\epsilon)}$ are given by

$$\mu^{(0)} = 1, \quad \mu^{(\epsilon)} = -\ln(2\mathbf{S}^{(0)} : \mathbf{S}^{(0)})^{1/2}. \quad (\text{A3a,b})$$

Note that $|\epsilon \ln \dot{\gamma}| \ll 1$ is preconditioned but it would be violated when $\dot{\gamma} \ll 1$, in particular at locations sufficiently far from the sphere. The domain where (A2) is valid would be wider for smaller ϵ . The $O(\epsilon^0)$ governing equations are

$$\nabla \cdot \mathbf{u}^{(0)} = 0, \quad -\nabla p^{(0)} + \nabla^2 \mathbf{u}^{(0)} = \mathbf{0}. \quad (\text{A4a,b})$$

The solutions to (A4a,b) with the boundary conditions (2.8a,b) are the well-known ones of Newtonian creeping flow, namely

$$\mathbf{u}^{(0)} = \mathbf{e}_r \frac{\cos \theta}{r} - \mathbf{e}_\theta \frac{\sin \theta}{2r}, \quad p^{(0)} = \frac{\cos \theta}{r^2}. \quad (\text{A5a,b})$$

The $O(\epsilon^1)$ governing equations are

$$\nabla \cdot \mathbf{u}^{(\epsilon)} = 0, \quad -\nabla p^{(\epsilon)} + \nabla^2 \mathbf{u}^{(\epsilon)} + \nabla \cdot (2\mu^{(\epsilon)} \mathbf{S}^{(0)}) = \mathbf{0}. \quad (\text{A6a,b})$$

The boundary conditions are

$$\left. \begin{aligned} \mathbf{e}_r \cdot \mathbf{u}^{(\epsilon)} &= 0, \quad \mathbf{e}_r \cdot \boldsymbol{\tau}^{(\epsilon)} \cdot \mathbf{e}_\theta = 0 \text{ at } r = 1, \\ \mathbf{u}^{(\epsilon)} &\rightarrow \mathbf{0}, \quad p^{(\epsilon)} \rightarrow 0 \text{ as } r \rightarrow \infty, \end{aligned} \right\} \quad (\text{A7})$$

Drag force on an oscillatory spherical bubble

where

$$\boldsymbol{\tau}^{(\epsilon)} = 2\mathbf{S}^{(\epsilon)} + 2\mu^{(\epsilon)}\mathbf{S}^{(0)}. \tag{A8}$$

From (A3a,b), the $O(\epsilon^1)$ viscosity, that contributes to the drag force, is given by

$$\mu^{(\epsilon)} = -\frac{\ln 3}{2} + 2 \ln r - \frac{\ln(\cos^2 \theta)}{2} = \left(\frac{2 - \ln 3}{2} + 2 \ln r\right) P_0(\cos \theta) - \frac{5}{3} P_2(\cos \theta) + \dots, \tag{A9}$$

where $P_n(\dots)$ is the n th-order Legendre polynomial. The solutions to (A6a,b) with (A7) and (A9) are

$$\left. \begin{aligned} \mathbf{u}^{(\epsilon)} &= \mathbf{e}_r \left(-\frac{2 \ln r}{r} + \frac{1}{3r} - \frac{1}{3r^3}\right) P_1(\cos \theta) + \mathbf{e}_\theta \left(\frac{\ln r}{r} + \frac{5}{6r} - \frac{1}{6r^3}\right) P_1^1(\cos \theta) + \dots, \\ p^{(\epsilon)} &= \left(\frac{11}{3r^2} - \frac{\ln 3}{2r^2}\right) P_1(\cos \theta) + \dots, \end{aligned} \right\} \tag{A10}$$

where $P_n^1(\cos \theta) = -dP_n(\cos \theta)/d\theta$. The drag force is given by

$$F = -2\pi \int_0^\pi \sigma_{rr}|_{r=1} \cos \theta \sin \theta \, d\theta, \tag{A11}$$

where σ_{rr} is the normal stress given by

$$\sigma_{rr} = -p + \mathbf{e}_r \cdot \boldsymbol{\tau} \cdot \mathbf{e}_r, \quad \sigma_{rr} = \sigma_{rr}^{(0)} + \epsilon \sigma_{rr}^{(\epsilon)}. \tag{A12a,b}$$

From (A5a,b), (A8) and (A10), the $O(\epsilon^0)$ and $O(\epsilon^1)$ normal stresses on the sphere wall are

$$\sigma_{rr}^{(0)}|_{r=1} = -3P_1(\cos \theta), \quad \sigma_{rr}^{(\epsilon)}|_{r=1} = \left(-7 + \frac{3 \ln 3}{2}\right) P_1(\cos \theta) + \dots. \tag{A13a,b}$$

From (A11), (A12a,b) and (A13a,b), the drag force with the power-law index $n \approx 1$ is approximated by

$$F = 4\pi + \left(\frac{28\pi}{3} - 2\pi \ln 3\right) (1 - n). \tag{A14}$$

Note that the analytical result of (A14) has been included in figure 2(b) to validate the credibility of the simulations.

Appendix B. The case of β_k included in the BF formula (3.4) for the Newtonian potential flow and for the Newtonian Stokes flow

For a potential flow around a sphere travelling with speed of $U = 1$ in a resting fluid, the velocity \mathbf{u} , the vorticity $\boldsymbol{\omega}$ and the components of the strain rate tensor \mathbf{S} are

$$\left. \begin{aligned} \mathbf{u} &= \mathbf{e}_r \frac{\cos \theta}{r^3} + \mathbf{e}_\theta \frac{\sin \theta}{2r^3}, \quad \boldsymbol{\omega} = \mathbf{0}, \\ S_{rr} &= -\frac{3 \cos \theta}{r^4}, \quad S_{\theta\theta} = S_{\phi\phi} = \frac{3 \cos \theta}{2r^4}, \quad S_{r\theta} = S_{\theta r} = -\frac{3 \sin \theta}{2r^4}. \end{aligned} \right\} \tag{B1}$$

Substituting (B1) into (3.5) gives

$$\beta_1(\mathbf{u}) = 12\pi, \quad \beta_2(\mathbf{u}) = 0, \quad \beta_3(\mathbf{u}) = 12\pi. \tag{B2a-c}$$

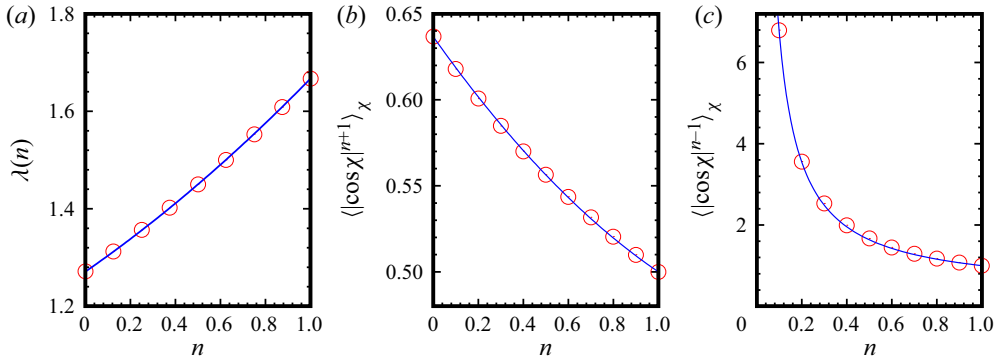


Figure 13. Profiles of (a) $\lambda(n)$ (defined in (3.9)), (b) $\langle |\cos \chi|^{n+1} \rangle_\chi$ and (c) $\langle |\cos \chi|^{n-1} \rangle_\chi$ as functions of $n(\in (0, 1))$. The circle symbols indicate the numerically integrated data. The solid curves correspond to the empirical formulae (C2), (C4) and (C6), respectively, for (a), (b) and (c).

For a steady Newtonian Stokes flow induced by a FS sphere, the quantities are

$$\left. \begin{aligned} \mathbf{u} &= \mathbf{e}_r \frac{\cos \theta}{r} - \mathbf{e}_\theta \frac{\sin \theta}{2r}, & \boldsymbol{\omega} &= -\mathbf{e}_\phi \frac{\sin \theta}{r^2}, \\ S_{rr} &= -\frac{\cos \theta}{r^2}, & S_{\theta\theta} &= S_{\phi\phi} = \frac{\cos \theta}{2r^2}, & S_{r\theta} &= S_{\theta r} = 0. \end{aligned} \right\} \quad (\text{B3})$$

Substituting (B3) into (3.5) gives

$$\beta_1(\mathbf{u}) = 4\pi, \quad \beta_2(\mathbf{u}) = \frac{8\pi}{3}, \quad \beta_3(\mathbf{u}) = \frac{4\pi}{3}. \quad (\text{B4a-c})$$

Appendix C. Approximated expressions for $\lambda(n)$, $\langle |\cos \chi|^{n+1} \rangle_\chi$ and $\langle |\cos \chi|^{n-1} \rangle_\chi$

For convenient use of (3.12) and (3.15), some approximated expressions as a function of the power-law index $n(\in (0, 1))$ will be shown. For $\lambda(n)$ defined in (3.9), fitting to the numerically integrated data (corresponding to the circle symbols in figure 13a) and the analytical values at the boundaries

$$\left. \begin{aligned} \lambda(0) &= \frac{1}{2} \int_{-1}^1 (1 + 2\zeta^2)^{1/2} d\zeta = \frac{\sqrt{3}}{2} + \frac{\sqrt{2}}{4} \ln(\sqrt{2} + \sqrt{3}), \\ \lambda(1) &= \frac{1}{2} \int_{-1}^1 (1 + 2\zeta^2) d\zeta = \frac{5}{3}, \end{aligned} \right\} \quad (\text{C1})$$

we obtain a formula

$$\lambda(n) = 0.076n^2 + 0.32n + 1.271. \quad (\text{C2})$$

For $\langle |\cos \chi|^{n+1} \rangle_\chi$, imposing the analytical values at the boundaries

$$\langle |\cos \chi|^{n+1} \rangle_\chi = \begin{cases} \frac{2}{\pi} & \text{for } n = 0 \\ \frac{1}{2} & \text{for } n = 1 \end{cases}, \quad (\text{C3})$$

we obtain a fitted formula

$$\langle |\cos \chi|^{n+1} \rangle_\chi = \frac{2}{\pi}(1 - n) + \frac{n}{2} - 0.048n(1 - n). \quad (\text{C4})$$

See figure 13(b) for the applicability of (C4).

Drag force on an oscillatory spherical bubble

For $\langle |\cos \chi|^{n-1} \rangle_\chi$, from two asymptotic solutions

$$\langle |\cos \chi|^{n-1} \rangle_\chi \rightarrow \begin{cases} \frac{2}{\pi} \left(\frac{1}{n} + \log 2 \right) & \text{for } n \rightarrow 0, \\ 1 - (n-1) \log 2 & \text{for } n \rightarrow 1, \end{cases} \quad (\text{C5})$$

we may draw an empirical expression

$$\langle |\cos \chi|^{n-1} \rangle_\chi = \frac{2}{\pi n} + 1 - \frac{2}{\pi}, \quad (\text{C6})$$

which well captures the numerically integrated data (see [figure 13c](#)).

REFERENCES

- ACHARYA, A., MASHELKAR, R.A. & ULBRECHT, J. 1977 Mechanics of bubble motion and deformation in non-Newtonian media. *Chem. Engng Sci.* **32**, 863–872.
- AGI, A., JUNIN, R., ABBAS, A., GBADAMOSI, A. & AZLI, N.B. 2020 Influence of ultrasonic on the flow behavior and disperse phase of cellulose nano-particles at fluid–fluid interface. *Nat. Resour. Res.* **29**, 1427–1446.
- AMSDEN, A.A. & HARLOW, F.H. 1970 A simplified MAC technique for incompressible fluid flow calculations. *J. Comput. Phys.* **6**, 322–325.
- ANDRIENKO, Y.A., SIGINER, D.A. & YANOVSKY, Y.G. 2000 Resonance behavior of viscoelastic fluids in Poiseuille flow and application to flow enhancement. *Intl J. Non-Linear Mech.* **35**, 95–102.
- BARNES, H.A., TOWNSEND, P. & WALTERS, K. 1969 Flow of non-Newtonian liquids under a varying pressure gradient. *Nature* **224**, 585–587.
- BARNES, H.A., TOWNSEND, P. & WALTERS, K. 1971 On pulsatile flow of non-Newtonian liquids. *Rheol. Acta* **10**, 517–527.
- BOBADE, V., BAUDEZ, J.C., EVANS, G. & ESHTIAGHI, N. 2017 Impact of gas injection on the apparent viscosity and viscoelastic property of waste activated sewage sludge. *Water Res.* **114**, 296–307.
- CASANELLAS, L. & ORTIN, J. 2011 Laminar oscillatory flow of Maxwell and Oldroyd-B fluids: theoretical analysis. *J. Non-Newtonian Fluid Mech.* **166**, 1315–1326.
- CASANELLAS, L. & ORTÍN, J. 2012 Experiments on the laminar oscillatory flow of wormlike micellar solutions. *Rheol. Acta* **51**, 545–557.
- CHHABRA, R.P. 1998 Rising velocity of a swarm of spherical bubbles in power law fluids at high Reynolds numbers. *Can. J. Chem. Engng* **76**, 137–140.
- CHHABRA, R.P. 2006 *Bubbles, Drops, and Particles in Non-Newtonian Fluids*. CRC.
- DE CORATO, M., DIMAKOPOULOS, Y. & TSAMOPOULOS, J. 2019a The rising velocity of a slowly pulsating bubble in a shear-thinning fluid. *Phys. Fluids* **31**, 083103.
- DE CORATO, M., SAINT-MICHEL, B., MAKRIORGOS, G., DIMAKOPOULOS, Y., TSAMOPOULOS, J. & GARBIN, V. 2019b Oscillations of small bubbles and medium yielding in elastoviscoplastic fluids. *Phys. Rev. Fluids* **4**, 073301.
- DEKKE, D., CARREAU, P.J. & MORDARSKI, J. 1986 Bubble velocity and coalescence in viscoelastic liquids. *Chem. Engng Sci.* **41**, 2273–2283.
- DESHPANDE, N.S. & BARIGOU, M. 2001 Vibrational flow of non-Newtonian fluids. *Chem. Engng Sci.* **56**, 3845–3853.
- DEYSARKAR, A.K. & TURNER, G.A. 1981 Flow of paste in a vibrated tube. *J. Rheol.* **25**, 41–54.
- DHOLE, S.D., CHHABRA, R.P. & ESWARAN, V. 2007a Drag of a spherical bubble rising in power law fluids at intermediate Reynolds numbers. *Ind. Engng Chem. Res.* **46**, 939–946.
- DHOLE, S.D., CHHABRA, R.P. & ESWARAN, V. 2007b Mass transfer from a spherical bubble rising in power-law fluids at intermediate Reynolds numbers. *Intl Commun. Heat Mass Transfer* **34**, 971–978.
- ELLER, A. 1968 Force on a bubble in a standing acoustic wave. *J. Acoust. Soc. Am.* **43**, 170–171.
- GAUDRON, R., WARNEZ, M.T. & JOHNSEN, E. 2015 Bubble dynamics in a viscoelastic medium with nonlinear elasticity. *J. Fluid Mech.* **766**, 54–75.
- GU, D. & TANNER, R.I. 1985 The drag on a sphere in a power-law fluid. *J. Non-Newtonian Fluid Mech.* **17**, 1–12.
- GUPTA, S., PATEL, S.A. & CHHABRA, R.P. 2020 Pulsatile flow of power-law fluids over a heated cylinder: flow and heat transfer characteristics. *Intl J. Therm. Sci.* **152**, 106330.

- GUPTA, S., PATEL, S.A. & CHHABRA, R.P. 2021 Effect of sinusoidally varying flow of yield stress fluid on heat transfer from a cylinder. *J. Heat Transfer* **143**, 061802.
- HIROSE, T. & MOO-YOUNG, M. 1969 Bubble drag and mass transfer in non-newtonian fluids: creeping flow with power-law fluids. *Can. J. Chem. Engng* **47**, 265–267.
- IWAMURO, M., WATAMURA, T. & SUGIYAMA, K. 2019 The influence of ultrasound irradiation on falling sphere in pseudo-plastic fluid. *Jpn. J. Multiphase Flow* **33**, 87–95.
- IWATA, S., YAMADA, Y., TAKASHIMA, T. & MORI, H. 2008 Pressure-oscillation defoaming for viscoelastic fluid. *J. Non-Newtonian Fluid Mech.* **151**, 30–37.
- JAMBURIDZE, A., DE CORATO, M., HUERRE, A., POMMELLA, A. & GARBIN, V. 2017 High-frequency linear rheology of hydrogels probed by ultrasound-driven microbubble dynamics. *Soft Matt.* **13**, 3946–3953.
- JOSEPH, D.D. 2006 Potential flow of viscous fluids: historical notes. *Intl J. Multiphase Flow* **32**, 285–310.
- KANG, I.S. & LEAL, L.G. 1988 The drag coefficient for a spherical bubble in a uniform streaming flow. *Phys. Fluids* **31**, 233–237.
- KARAPETSAS, G., PHOTEINOS, D., DIMAKOPOULOS, Y. & TSAMOPOULOS, J. 2019 Dynamics and motion of a gas bubble in a viscoplastic medium under acoustic excitation. *J. Fluid Mech.* **865**, 381–413.
- KISHORE, N., CHHABRA, R.P. & ESWARAN, V. 2007 Mass transfer from a single fluid sphere to power-law liquids at moderate Reynolds numbers. *Chem. Engng Sci.* **62**, 6040–6053.
- KULKARNI, A.A. & JOSHI, J.B. 2005 Bubble formation and bubble rise velocity in gas-liquid systems: a review. *Ind. Engng Chem. Res.* **44**, 5873–5931.
- LANDAU, L.D. & LIFSHITZ, E.M. 1987 *Course of Theoretical Physics. Vol. 6: Fluid Mechanics*. Pergamon.
- LIU, Y., SUGIYAMA, K. & TAKAGI, S. 2016 On the interaction of two encapsulated bubbles in an ultrasound field. *J. Fluid Mech.* **804**, 58–89.
- MAGNAUDET, J. & EAMES, I. 2000 The motion of high-Reynolds-number bubbles in inhomogeneous flows. *Annu. Rev. Fluid Mech.* **32**, 659–708.
- MAJDALANI, J. & VAN MOORHEM, W.K. 1997 Multiple-scales solution to the acoustic boundary layer in solid rocket motors. *J. Propul. Power* **13**, 186–193.
- MCCLEMENTS, D.J. 2004 *Food Emulsions: Principles, Practices, and Techniques*. CRC.
- MENDOZA-FUENTES, A.J., CEDEÑO MADERA, R., MORENO, L., ZENIT, R., MENA, B. & MANERO, O. 2018 A note on the effect of ultrasonic waves on droplets rising in Newtonian and non-Newtonian fluids. *Fluid Mech. Res. Intl* **2**, 171–175.
- MICHAELIDES, E. 2006 *Particles, Bubbles & Drops: Their Motion, Heat and Mass Transfer*. World Scientific.
- MISHRA, G. & CHHABRA, R.P. 2021 Influence of flow pulsations and yield stress on heat transfer from a sphere. *Appl. Math. Model.* **90**, 1069–1098.
- MISHRA, G., PATEL, S.A. & CHHABRA, R.P. 2020 Pulsatile flow of power-law fluids over a sphere: momentum and heat transfer characteristics. *Powder Technol.* **360**, 789–817.
- MISSIRLIS, K.A., ASSIMACOPOULOS, D., MITSOULIS, E. & CHHABRA, R.P. 2001 Wall effects for motion of spheres in power-law fluids. *J. Non-Newtonian Fluid Mech.* **96**, 459–471.
- MOYERS-GONZALEZ, M.A., OWENS, R.G. & FANG, J. 2009 On the high frequency oscillatory tube flow of healthy human blood. *J. Non-Newtonian Fluid Mech.* **163**, 45–61.
- MÜLLER, B. & CHAN, C. 2019 An FFT-based solution method for the Poisson equation on 3D spherical polar grids. *Astrophys. J.* **870**, 43–51.
- OHTA, M., IWASAKI, E., OBATA, E. & YOSHIDA, Y. 2003 A numerical study of the motion of a spherical drop rising in shear-thinning fluid systems. *J. Non-Newtonian Fluid Mech.* **116**, 95–111.
- OHTA, M., IWASAKI, E., OBATA, E. & YOSHIDA, Y. 2005 Dynamic processes in a deformed drop rising through shear-thinning fluids. *J. Non-Newtonian Fluid Mech.* **132**, 100–107.
- PHAN-THIEN, N. & DUDEK, J. 1982a Pulsating flow of a plastic fluid. *Nature* **296**, 843–844.
- PHAN-THIEN, N. & DUDEK, J. 1982b Pulsating flow revisited. *J. Non-Newtonian Fluid Mech.* **11**, 147–161.
- PREMLATA, A.R., TRIPATHI, M.K., KARRI, B. & SAHU, K.C. 2017 Numerical and experimental investigations of an air bubble rising in a Carreau-Yasuda shear-thinning liquid. *Phys. Fluids* **29**, 033103.
- RADL, S., TRYGGVASON, G. & KHINAST, J.G. 2007 Flow and mass transfer of fully resolved bubbles in non-Newtonian fluids. *AIChE J.* **53**, 1861–1878.
- RENAUD, M., MAURET, E. & CHHABRA, R.P. 2004 Power-law fluid flow over a sphere: average shear rate and drag coefficient. *Can. J. Chem. Engng* **82**, 1066–1070.
- RYSKIN, G. & LEAL, L.G. 1984 Numerical solution of free-boundary problems in fluid mechanics. Part 1. The finite-difference technique. *J. Fluid Mech.* **148**, 1–17.
- SAMARAS, K., KOSTOGLU, M., KARAPANTSIOS, T.D. & MAVROS, P. 2014 Effect of adding glycerol and Tween 80 on gas holdup and bubble size distribution in an aerated stirred tank. *Colloids Surf. A Physicochem. Eng. Asp.* **441**, 815–824.

Drag force on an oscillatory spherical bubble

- SELWAY, N., CHAN, V. & STOKES, J.R. 2017 Influence of fluid viscosity and wetting on multiscale viscoelastic lubrication in soft tribological contacts. *Soft Matt.* **13**, 1702–1715.
- SERRIN, J. 1959 Mathematical principles of classical fluid mechanics. In *Fluid Dynamics I/Strömungsmechanik I*, pp. 125–263. Springer.
- SIGINER, A. 1991 On the pulsating pressure gradient driven flow of viscoelastic liquids. *J. Rheol.* **35**, 271–311.
- SLATTERY, J.C. & BIRD, R.B. 1961 Non-Newtonian flow past a sphere. *Chem. Engng Sci.* **16**, 231–241.
- SONG, D., GUPTA, R.K. & CHHABRA, R.P. 2011 Drag on a sphere in Poiseuille flow of shear-thinning power-law fluids. *Ind. Engng Chem. Res.* **50**, 13105–13115.
- STEIN, S. & BUGGISCH, H. 2000 Rise of pulsating bubbles in fluids with a yield stress. *Z. Angew. Math. Mech.* **80**, 827–834.
- STONE, H.A. 1993 An interpretation of the translation of drops and bubbles at high Reynolds numbers in terms of the vorticity field. *Phys. Fluids A* **5**, 2567–2569.
- SUGIYAMA, K. & TAKEMURA, F. 2010 On the lateral migration of a slightly deformed bubble rising near a vertical plane wall. *J. Fluid Mech.* **662**, 209–231.
- WANG, Z., WANG, H. & GUO, Q. 2006 Effect of ultrasonic treatment on the properties of petroleum coke oil slurry. *Energy Fuels* **20**, 1959–1964.
- WELLEK, R.M. & GÜRKAN, T. 1976 Mass transfer to drops moving through power law fluids in the intermediate Reynolds number region. *AIChE J.* **22**, 484–490.
- YANG, S.M. & LEAL, L.G. 1991 A note on memory-integral contributions to the force on an accelerating spherical drop at low Reynolds number. *Phys. Fluids A* **3**, 1822–1824.
- ZARE, M., DANESHI, M. & FRIGAARD, I.A. 2021 Effects of non-uniform rheology on the motion of bubbles in a yield-stress fluid. *J. Fluid Mech.* **919**, A25.
- ZHANG, L., YANG, C. & MAO, Z.S. 2010 Numerical simulation of a bubble rising in shear-thinning fluids. *J. Non-Newtonian Fluid Mech.* **165**, 555–567.